Ab initio treatment of silicon-hydrogen bond rupture at Si/SiO_2 interfaces

Markus Jech,[1,*] Al-Moatasem El-Sayed,[1,2,†] Stanislav Tyaginov,[1,3,‡] Alexander L. Shluger,[4,§] and Tibor Grasser[1,‖]

[1]*Institute for Microelectronics, Technische Universität Wien, A-1040 Vienna, Austria*

[2]*Nanolayers Research Computing, Ltd., 1 Granville Court, Granville Road, London N12 0HL, United Kingdom*

[3]*imec, Kapeldreef 75, B-3001 Leuven, Belgium*

[4]*Department of Physics and Astronomy and London Centre for Nanotechnology, University College London, Gower Street, London WC1E 6BT, United Kingdom*

(Received 15 March 2019; revised manuscript received 31 July 2019; published 5 November 2019)

Even after more than 50 years of development, a major issue in silicon-based technology is the understanding of the Si/SiO_2 interface and its defects, particularly the unsaturated silicon dangling bonds which have to be passivated by hydrogen during fabrication. Although it is well known that hydrogen dissociation from an initially passivated interfacial Si dangling bond results in an electrically active defect, there is still no consensus on the actual microscopic Si–H bond-breaking mechanism, despite a significant research effort. The most thorough theoretical study in the field was published by Tuttle and Van de Walle 20 years ago. Although it was then suggested that the hydrogen dissociates most likely into a bond-center site, no clean argument for bond rupture could be given at that time. In order to take a fresh look at this highly important problem, we employ the latest *ab initio* methods available, including the method of well-tempered metadynamics and nudged-elastic-band calculations based on density functional theory (DFT). This allows us to study the interactions of a Si–H bond with its realistic environment in a three-dimensional $Si/a\text{-}SiO_2$ interface in considerable detail. Using classical force fields and well-tempered metadynamics in conjunction with DFT, we provide new insights into the dissociation kinetics. We find that one of the previously suggested dissociation paths only leads into a neutral, metastable state which would not facilitate bond dissociation. By sampling the configuration space in greater detail than ever before, we propose a trajectory whereby the H first moves towards an adjacent Si and in a second step relaxes into a configuration between the next-nearest Si–Si bond. The final statistical analysis on a large number of defects on this amorphous interface yields potential energy surfaces and barriers which are in excellent agreement with experimental values.

DOI: 10.1103/PhysRevB.100.195302

I. INTRODUCTION

Structural disorder and material defects have received a significant amount of interest due to their diverse implications and manifold applications. Particularly in the field of micro- and nanoelectronics, defects are of enormous importance for semiconductor applications like modern metal-oxide-semiconductor field-effect transistors (MOSFETs). Point defects not only determine electrical and optical properties but also impose limits on the device reliability by creating localized trapping sites for electrons and holes. Among the various defect configurations observed in modern electronic devices, hydrogen—in one of its many forms—and its interaction with the surrounding network is of special interest due to its role as a key ingredient in a wide range of technologies. Numerous studies have shown that hydrogen leads to the formation of defects within amorphous oxides [1–5], in addition to the pre-existing intrinsic active states associated with these materials [1,6,7]. On the other hand, hydrogen is well known to passivate electrically active states, which is essential for producing solar cells [8] and silicon-based transistors. Additionally, its ability to relieve strain and its influence on surface reconstruction allows the development of emerging technologies beyond complementary metal-oxide semiconductor (CMOS) applications [9–11].

The deliberate introduction of hydrogen into semiconductor devices during fabrication initially improves their characteristics by annealing a particular type of defect at the Si/SiO_2 interface known as the P_b center. Using electron-spin-resonance spectroscopy, two electrically active types of P_b defects have been clearly identified on the industrially most relevant ⟨100⟩ surface, called P_{b0} and P_{b1} [6,12–14]. While the structural properties of the P_{b1} center are still controversial [15–17], the dominant P_{b0} center has been identified as a trivalent interfacial Si back bonded to three Si atoms in the bulk [18,19], rendering it consistent with a silicon dangling bond (Si-DB) in the silicon subinterfacial region. However, it was shown that the passivation process can actually be reversed by thermal dissociation [20,21], the interaction with energetic carriers [22–24], and even during device operation [25–31]. Thus, the dissociation of the Si–H bond plays a crucial role in reliability issues and requires a fundamental understanding of the involved kinetics.

*jech@iue.tuwien.ac.at
†elsayed@iue.tuwien.ac.at
‡tyaginov@iue.tuwien.ac.at
§a.shluger@ucl.ac.uk
‖grasser@iue.tuwien.ac.at

Experimental data by Brower and Stesmans show a process with an activation barrier between 2.5 and 2.8 eV [20,21]. The pioneering work of Tuttle *et al.* and Van de Walle *et al.* used *ab initio* calculations to investigate the structural and energetic properties of various configurations of hydrogen in periodic models of crystalline and amorphous Si [32–39] to explain Si–H bond rupture. They showed that dissociation via the stretching mode into free space requires 3.6 eV, the Si–H binding energy, which is too large to be consistent with experimental data. Instead, they proposed that by interactions with the surrounding network the dissociation barrier may be reduced. In agreement with experimental observations [40–42], they suggested that it would be more likely for neutral H to move into a Si–Si bond-center site (referred to as BC site) in bulk Si [43–45]. Being in the BC site, the H is placed between a strained Si–Si bond and is 1.75 to 2.5 eV higher in energy than the Si–H configuration, depending on whether the BC site is adjacent to a Si-DB or anywhere else in the bulk Si. However, only the different configurations have been investigated, and no dissociation pathway connecting the initial Si–H configuration and the final BC configuration could be given at that time. In Ref. [33], the authors speculated that by bending the H into the antibonding configuration (referred to as AB site), a 180° flipped position of the hydrogen, electrically active levels in the Si band gap allow the Si–H complex to become charged and the H to dissociate. However, these results are almost two decades old, and recent progress in DFT development and atomistic simulations allow a more accurate description which provides new insights, as we will show in the following.

While previous work has shown that the AB site is energetically higher than the equilibrium site and that the BC site would form a suitable configuration for H to diffuse away, this work and the presented results systematically address the remaining open questions: How exactly would the H eventually dissociate away from the Si at the Si/SiO_2 environment? To this aim we study how bond breakage occurs by employing various methods, from classical molecular dynamics to *ab initio* calculations, to characterize the Si–H bond at the Si/SiO_2 interface. The starting point of our study is a Si/SiO_2 structure with a silicon dangling bond at the interface which was passivated by hydrogen. In order to gain insight into the defect generation kinetics, we use a combination of state-of-the-art simulation techniques together with a realistic Si/a-SiO_2 interface model containing 475 atoms. We applied (well-tempered) metadynamics, an enhanced sampling technique, to simulate the free-energy surface within the vicinity of the interfacial Si–H bond. In addition to the stable configuration of the intact Si–H bond, two (meta-) stable configurations for the H atom, including the minimum energy paths connecting them, could be identified. By employing density functional theory calculations, we further investigated the Si–H kinetics and also assess the electronic properties for the various configurations to check how additional energy levels in the band gap may aid the dissociation process. These calculations clearly show that the previously suggested AB site is only a metastable state without energy levels in the Si band gap. As such, the AB site is a dead end in the reaction dynamics and would not facilitate breaking of the Si–H bond. However, our calculations clearly suggest a new dissociation pathway for interfacial Si–H bonds, which is also validated at a statistical level. Our results thus provide a more complete understanding of how defects at the Si/SiO_2 interface can be created.

II. CALCULATION DETAILS

We use a combination of classical interatomic potentials and DFT calculations applied on the Si–H bond within the three-dimensional environment of a Si/SiO_2 interface. Here, we give a detailed description of the different methods and their applications within this work.

A. DFT setup

All simulations were carried out using the CP2K package [46], a DFT code which uses a mixed Gaussian and plane-waves approach to represent the electrons in the system. Throughout this work, three-dimensional (3D) periodic boundary conditions were used for the Si/SiO_2 system. A double-ζ Gaussian basis set optimized for condensed-phase systems for Si, O, and H was employed in conjunction with the Goedecker-Teter-Hutter (GTH) pseudopotentials [47,48]. The plane-wave cutoff used in these calculations was set to 650 *Ry*. In order to minimize the errors in the band gaps and barrier calculations, the nonlocal, hybrid functional PBE0_TC_LRC was used. This functional contains a 20% contribution of Hartree-Fock exchange and correlation as well as using a truncated Coulomb operator with a cutoff radius set to 2 Å [49]. To mitigate the computational cost of calculating the Hartree-Fock integrals within the nonlocal functional, the auxiliary density matrix method (ADMM) was employed [50]. In addition to the main basis set, a more sparse auxiliary basis set (pFIT basis set for Si, O, and H) was used to calculate the Hartree-Fock exchange terms, which allows a reduction of computational expenses. The geometry optimizations were performed using the Broyden-Fletcher-Goldfarb-Shanno (BFGS) algorithm [51–54] to minimize forces on atoms to within 24 pN (1.5×10^{-2} eV/Å). Energy barriers between different atomistic configurations were calculated using the climbing-image nudged-elastic-band method (CI-NEB) [55,56]. The algorithm linearly interpolates between the initial and final configuration to generate a trajectory, connected by springs. The whole band is then simultaneously relaxed with the spring's force constant set to 19.5 eV/Å^2.

B. Si/SiO_2 interface creation

Constructing credible interface structures between amorphous oxides and a crystalline substrate has been proven to be an extremely challenging problem [57–62] due to the lack of detailed information regarding the microscopic interfacial region. It is known from measurements performed in thin SiO_2 films that thermal oxidation of silicon results in an intrinsic compressive stress within the oxide [63–67]. Depending on the oxide thickness and the oxidation temperature, the reported values are between 0.5 and 2.0 GPa. This stress is also observed in x-ray reflectivity experiments [68], which show an increased density of SiO_2 in an Si/SiO_2 system compared to bulk amorphous silica as well as a compressed Si–O–Si angle distribution [69,70]. Furthermore, transmission electron microscope [71,72] (TEM) images and atomic-scale

electron-energy-loss spectroscopy [73,74] (EELS) indicate a transition region of approximately 5–7 Å between crystalline silicon and the amorphous structure. Within this interfacial region the band gap as well as the dielectric constant continuously change between Si and SiO_2, as was also found in recent DFT studies [75,76]. Photoemission measurements were used to investigate the chemical structure of ultrathin interfaces [71,77]. The data suggest three transition layers with increasing concentration of partially oxidized silicon across the interface. All these experimental results provide constraints a realistic interface model must satisfy.

The methodology used to create a 3D periodic Si/SiO_2 interface model with two interface regions adapts the melt and quench procedure previously used to create a-SiO_2 cells [1,3]. Due to the excessive calculation steps required for reliable models within molecular dynamics (MD) simulations, the ReaxFF force field [78] implemented in the LAMMPS code [79] was used. Starting from a $3 \times 3 \times 3$ β-cristobalite cell, whose lateral cell dimensions were fixed to that of silicon, we minimized the energy by allowing the cell to move in the c direction. It was found that this procedure gives a density of $\sim 2.3\,\mathrm{g/cm^3}$, in agreement with measured values [71]. Subsequently, the cell dimensions were fixed during the melt and quench procedure. The first layer of Si atoms on either side was frozen while the remaining atoms were given random velocities from a Gaussian distribution. First, the system was equilibrated at 300 K for 10 ps using a Berendsen thermostat. Afterwards the temperature was linearly increased to 5000 K over 60 ps to melt SiO_2 and further equilibrated for an additional 100 ps, followed by a quench to 0 K at a rate of 1.6 K/ps. In the final step crystalline Si was added at the top and bottom of the model, undercoordinated atoms were passivated by hydrogen, and the structure was allowed to relax at 300 K. In total over 100 Si/SiO_2 models were created, which resulted in various defect configurations at the interface as well as in the oxide. The three most promising models, in terms of their geometrical properties such as coordination number, were chosen for this study and further examined as well as optimized using our DFT setup. Simulations of the nonoptimized interface indeed gave rise to an intrinsic stress of 3.5 GPa, as mentioned above. Thus, in order to obtain a more realistic interface model for our subsequent DFT simulations, we applied an external pressure of 1 GPa parallel to the interface and performed a full cell optimization including the ionic positions of the model where the initial tetragonal cell symmetry was kept fixed. All three structures converged to almost the same cell size, $a = b = 16.203$ Å, $c = 32.965$ Å, with a variance of 0.007 Å in the lateral dimensions and 0.014 Å in the c direction.

The extracted geometrical properties of the final interface models are in good agreement with experimental data. The Si–O bond length ranges from 1.46 to 1.84 Å(ReaxFF: 1.52–2.04 Å) and peaks at around 1.64 Å(ReaxFF: 1.61 Å), which is consistent with infrared absorption measurements [71]. The Si–O–Si angle averages at 133.5° (ReaxFF: 121.4°), which agrees well with the conclusions reached in Ref. [70], that the angle is reduced to 135° compared to 148° in bulk structures, while the O–Si–O angles remain almost unchanged compared to bulk SiO_2 (∼109°, ReaxFF: ∼109°). To further quantify the quality of the interface, we calculated the deformation of the

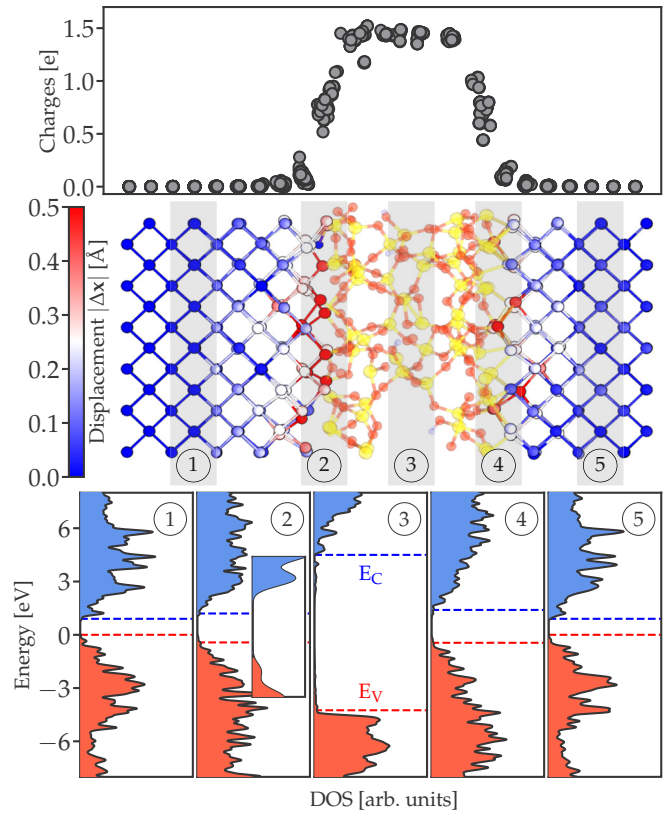

FIG. 1. A density functional theory simulation of the chosen Si/a-SiO_2/Si interface structure containing 475 atoms. The upper panel shows the charges calculated with Mulliken population analysis across the interface model. One can see a gradual change from elemental silicon to fully oxidized silicon with the first 2–3 transition layers. The middle panel shows the interface model and the displacement of the Si atoms from their respective equilibrium position in c-Si. Blue (dark atoms in region 1 and 5) means a displacement of less than 0.2 Å, while the highlighted red atoms (dark atoms in region 2 and 4) at the interface are strongly displaced. The bottom panel shows the density of states at different positions across the slab. Our results are in good agreement with well-established results. The band gap of Si as well as of a-SiO_2 is underestimated by about ∼10% (compared to $E_{g,Si} = 1.12$ eV and $E_{g,SiO_2} = 9.1$ eV). For interpretation of the references to color in this figure legend, the reader is referred to the web version of this article.

c-Si lattice as the deviation of the atomic positions from their respective positions in crystalline silicon, see Fig. 1 (middle panel). One can clearly see that already three layers away from the Si/SiO_2 interface the crystal structure is almost completely restored, with displacements less than 0.2 Å. However, directly at the transition layer, distortions are stronger due to the formation of Si–O bonds, giving rise to a higher strain at the direct interface between Si and SiO_2. In addition to the structural quality we also analyzed the electronic structure of the interface system. Figure 1 (upper panel) shows the oxidation state of silicon atoms across the Si/SiO_2 model using Mulliken population analysis. The profile clearly shows a gradual change from Si^0 in the crystalline Si part to its fully oxidized form Si^{+4} (which corresponds to a net charge of $\sim 1.4e$ in our DFT setup) in the SiO_2 region over a ∼5-Å transition region, which is qualitatively very similar to the results

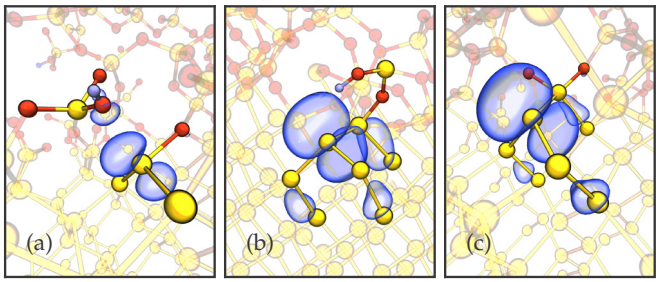

FIG. 2. Three examples of silicon dangling bond interface defects created within the Si/SiO_2 interface models. Configuration (a) at a first glance is consistent with a P_{b1} center (back bonded to two Si and one O atom). The spin density suggests that the defect state is mainly a nonbinding p orbital, which contradicts experimental results [12,13,18] and therefore was not further considered. Configurations like (b) have an extra H next to the passivated defect which might distort the calculation results and were also not considered. Finally, configuration (c), where the unpassivated Si is trivalently bonded to three other Si's, with an sp^3 hybridized dangling bond orbital, appeared closest to the well-known P_{b0} center and was used in this study.

of Ref. [77]. This is also reflected in the calculated density of states (DOS) across the model, see Fig. 1 (lower panels). While in the bulk regions (1, 3, and 5) the corresponding band gaps (0.95 and 8.58 eV) compare well to the known values (1.1 eV for Si and 8.9 eV for a-SiO_2), one can see a continuous change of the band gap within the interfacial regions (2 and 4). Furthermore, one can see additional electronic states within the band gap for the interface (2 and 4) and the bulk SiO_2 (3) regions. These induced states can be identified as silicon-band wave functions extending into the near oxide region. Such features have also been reported in recent experimental studies [73,74], where the authors conclude that this limits the practical oxide thickness to 1.2 nm. It may be inferred that within our interface model, having an oxide thickness of 1.1 nm, even region 3 does not exhibit actual full bulk SiO_2 properties.

The preselected (using ReaxFF) and optimized (using DFT) interface models possess three different silicon dangling bond configurations (which were passivated by H) at the interface; see examples in Fig. 2. From electron-spin-resonance studies the characteristics of Si/SiO_2 interface defects, known to be P_b centers, are well known: A trivalent interfacial Si, back bonded to three Si atoms in the bulk with an sp^3 hybridized dangling bond orbital. As can be seen in Fig. 2, configurations like those in (c) fully meet these requirements and were therefore chosen for our study. Further structural details including the atomistic models as well as a defect analysis can be found in the Supplemental Material [80].

To summarize, we created different Si/SiO_2 interface structures by adapting the melt and quench procedure. While the equilibrated models using the ReaxFF force field are used as a starting point for our metadynamics simulations, further geometry and cell optimizations within our DFT setup provide fully relaxed models for the *ab initio* calculations, see Sec. III. Both methods give qualitatively similar results and properly reflect experimental observations such as an abrupt transition region, geometrical statistics, and the silicon oxidation state profile across the interface. Optimization using DFT even improved the geometrical analysis and also showed a good agreement of the calculated electronic structure with experiments. A recent study [81] investigated the applicability of ReaxFF to model glassy silica. The authors concluded that ReaxFF has a promising potential for creating and modeling amorphous systems and would even allow study of the surface reactivity, thanks to its ability to dynamically form and break bonds.

III. RESULTS

In order to establish the detailed kinetics responsible for the creation of silicon dangling bonds, we investigate the Si–H bond properties in a realistic Si/SiO_2 interface model. We employ well-tempered metadynamics using a classical force field to explore the potential landscape in the vicinity of the interfacial Si–H bond. Building on these results, we then investigate the Si–H dynamics more accurately by using DFT, which enables us to identify the most likely dissociation pathway for creating an interface defect.

A. Metadynamics

Well-tempered metadynamics allows one to sample the free-energy landscape in the direct vicinity of the Si–H bond by driving the system out of its equilibrium. Thus, this method is well suited for finding (meta-) stable configurations and dissociation pathways for the hydrogen at the interface. However, the large amount of simulation steps necessary to converge such a simulation, together with the rather large Si/SiO_2 model system, permits the use only of a classical force-field. We used the ReaxFF force field [78] implemented in LAMMPS [79] in combination with PLUMED [82]. As the starting point for these calculations we chose an equilibration phase for 100 ps at $T = 300$ K by assigning random, normally distributed velocities to the whole system. Subsequently, we ran well-tempered metadynamics simulations for different simulation times and bias factors to make sure that the results are converged. Within these simulations we defined two collective variables (CVs) which were biased and monitored during the calculations: the Si–H bond distance r as well as the polar angle ϕ with respect to its equilibrium configuration. The azimuthal angle, however, was only monitored and not explicitly biased within the metadynamics simulations. Furthermore, we restricted the bond distance to within 4 Å, which ensured sampling of the free-energy landscape only in the direct vicinity of the Si–H bond. Additional computational details are given in the Appendix.

The resulting free-energy landscape is shown in Fig. 3. A representation in 3D space is given in the upper panels of Fig. 3, which shows the isosurface for three values of the potential energy. In order to give a more intuitive picture of the free energy, we mapped the potential onto 2D space by only considering the CV r and the polar angle ϕ, see Fig. 3. Three distinct minima can be identified: (1) corresponds to the intact Si–H bond in its equilibrium configuration, (3) represents the H in the AB site, and (5) marks the newly identified minimum formed by the H being in the next but one BC site between Si_2 and Si_3.

The respective atomistic configurations are schematically illustrated in the right panel of Fig. 3. In addition, to extract

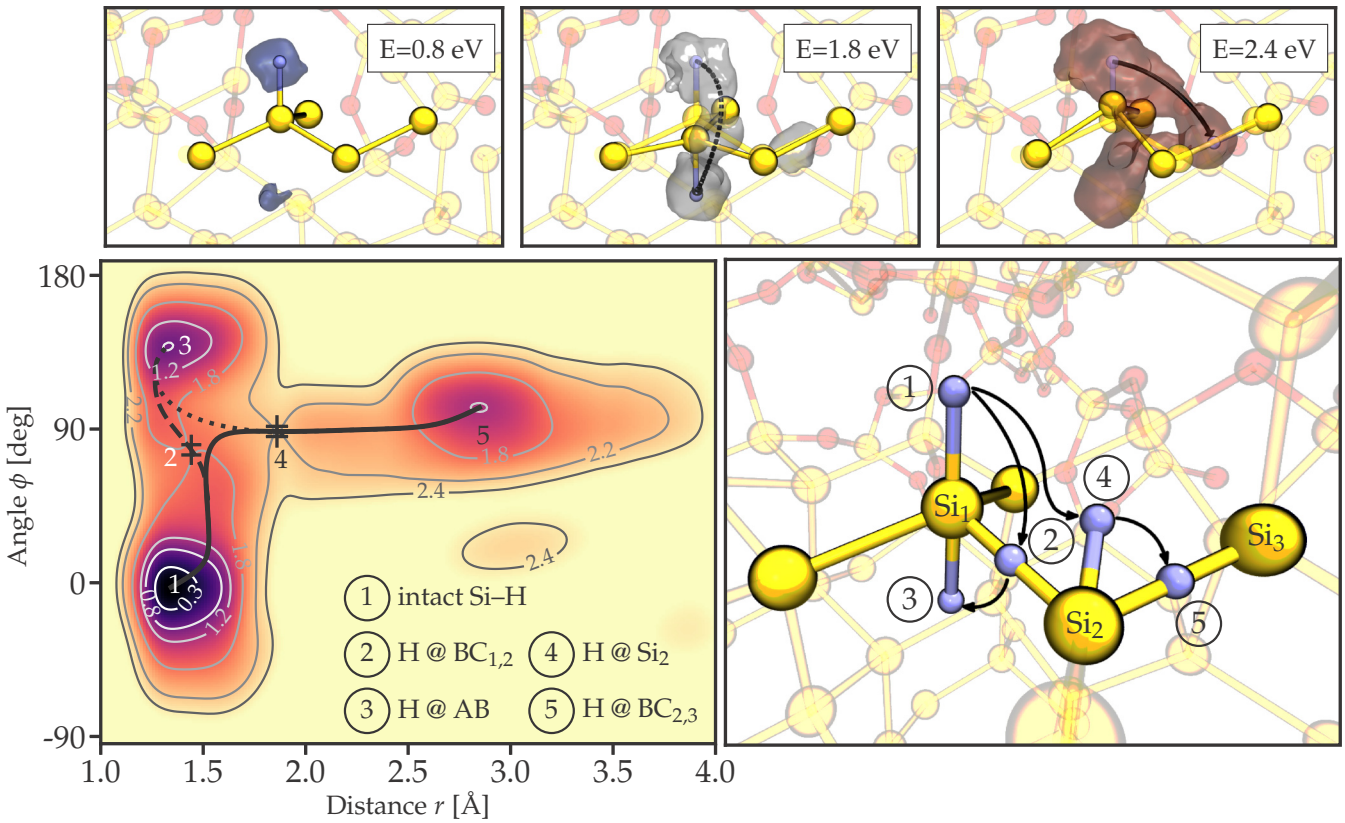

FIG. 3. The free-energy landscape (in a 3D and 2D representation) together with a schematic of the atomistic structure in the vicinity of the interfacial Si–H bond obtained from the ReaxFF force field. Three distinct minima are visible: The equilibrium position (1) at $r = 1.37$ Å and $\phi = 0°$, the H in the AB site labeled with (3), as well as the $BC_{2,3}$ configuration (5) where the H moved in between the Si_2–Si_3 bond. The crosses (2) and (4) mark the transition barriers for the minimum energy paths (lines) connecting the different minima.

the minimum energy paths (MEPs) connecting the different minimum configurations, we used more efficient CVs, such as $r' = 1/\sqrt{2}(r_{Si_3,H} - r_{Si_1,H})$ or simply the angle ϕ.

Inverting the H around Si_1 into the AB site (3), which is 0.8 eV higher in energy, proceeds via the dashed path in Fig. 3. The energy of the transition state is 1.75 eV, and its configuration corresponds to the H being in the $BC_{1,2}$ site (2). It is interesting to note that although the H forms a bond-center configuration between the Si_1–Si_2 bond, this is not a preferred and stable configuration for the H atom along the given path, contrary to the fact that in crystalline bulk Si the BC site is a stable configuration of H.

In addition, the hydrogen can be moved into the $BC_{2,3}$ configuration (5), shown as the solid black line in Fig. 3. The extracted MEP yields a transition state (4) where the H is stretched away from its initial Si (Si_1) and attached to the adjacent Si (Si_2). With a forward barrier of 2.25 eV and a backward barrier of 1.05 eV, this trajectory is a promising candidate to explain the measurement data in Ref. [83], which reports barrier heights of 2.83 and 1.51 eV for the forward and reverse process, respectively. The dotted line in Fig. 3 shows the MEP connecting the AB site (3) and the $BC_{2,3}$ configuration (5). No additional transition could be found, and thus the reaction would again proceed over state (4), making the AB site a dead end in the reaction dynamics.

B. DFT

To further investigate the Si–H kinetics and assess the electronic structure for the various configurations we employ DFT simulations. Building on the results of the metadynamics simulations, we ran CI-NEB calculations to identify the bond-breaking dynamics. The initial and final configurations obtained from the classical force-field calculations were used to construct a trajectory with 13 frames in total by using linear interpolation (note that this corresponds to a direct connection between the minima in Fig. 3). Subsequently, CI-NEB simulations optimized the band, including its endpoints.

1. Trajectory 1: Si–H → $BC_{2,3}$

First, we analyzed the direct path between the equilibrium Si–H configuration (1) and the $BC_{2,3}$ site (5) in more detail, as it appears most promising in terms of capturing the reaction dynamics. Figure 4 shows the resulting energy barrier along the calculated path together with the respective atomic structures and the projected DOS onto Si_1. The calculated trajectory possesses very similar features, as already observed in Fig. 3. The hydrogen first moves towards Si_2, marking the reaction barrier, and eventually moves in between the Si_2–Si_3 bond which was stretched from 2.34 to 3.13 Å, thereby forming a BC configuration. The total energy barrier along the direct trajectory which separates the intact Si–H configuration

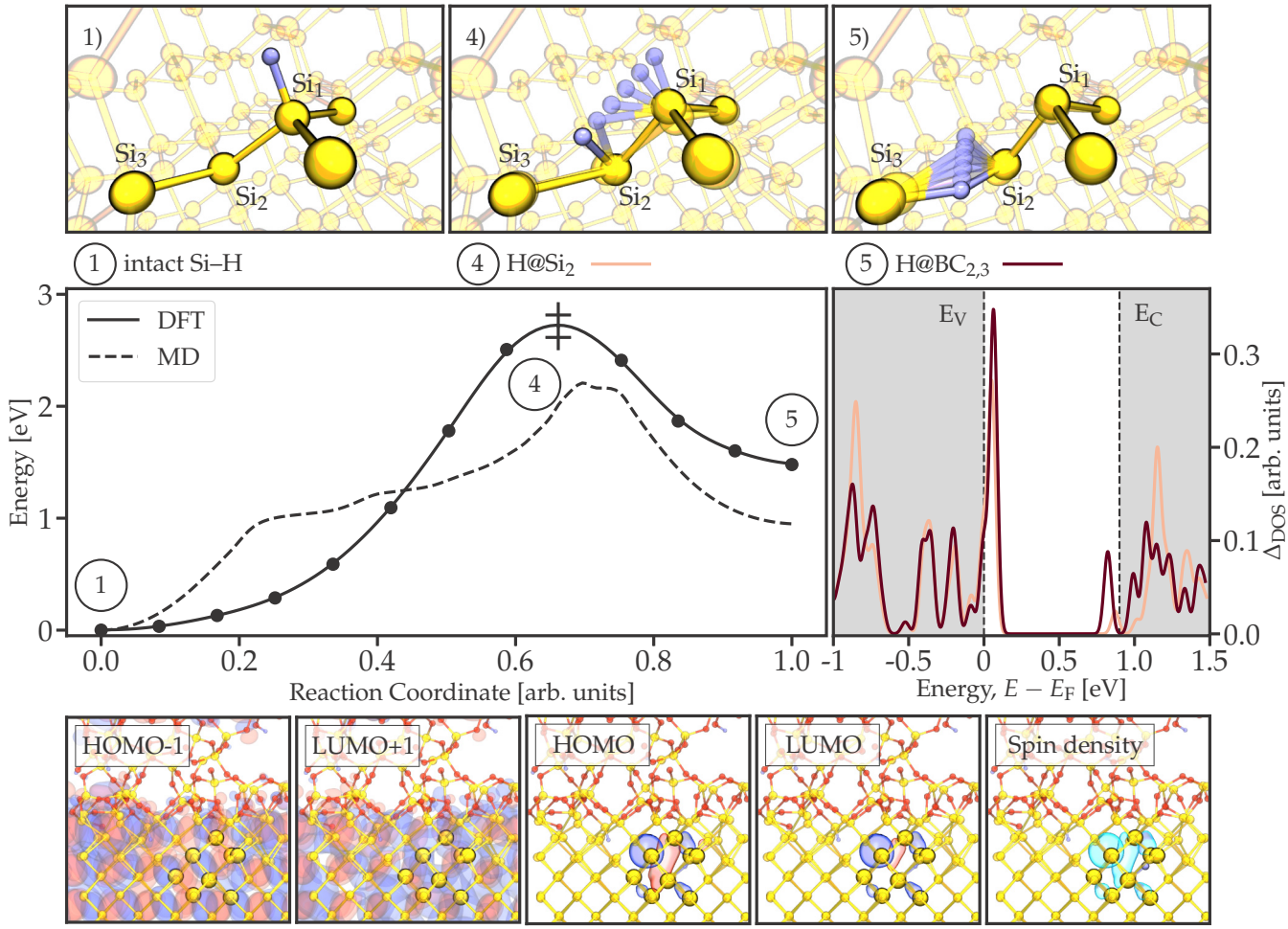

FIG. 4. A climbing image nudged-elastic-band (CI-NEB) simulation investigating the direct MEP connecting the intact Si–H configuration (1) and the next-nearest BC site between Si_2 and Si_3 (5) via the transition state (4) where the H is attached to the adjacent Si_2. The total energy required for the forward reaction is 2.77 and 1.30 eV for moving the H back to its initial configuration. The right panel shows the difference of the projected DOS onto the Si_1 atom compared to the intact Si-H configuration. It is clearly visible that the transition state and also the final state introduce localized electronic states in the Si band gap. Additionally, the lower panels show the resulting wave functions of the final state (5). The HOMO-1 and the LUMO + 1 orbital are delocalized Si band states (which, however, penetrate into the oxide region), whereas the HOMO and LUMO orbitals are localized around the Si-DB. The spin density suggests the dangling bond to be constituted by a slightly distorted unpaired Si sp^3 hybrid orbital.

and the $BC_{2,3}$ site is 2.77 eV for the forward reaction and 1.30 eV for repassivating the Si dangling bond. Compared to the classical force-field calculation, both values are even closer to the experimentally extracted barriers for breaking (2.83 eV) and passivating (1.51 eV) an interfacial Si–H bond. Furthermore, the transition state (4) and the final state (5) introduce a localized electronic level in the Si band gap, a filled state close to the valence band edge, as well as an empty level in the upper half of the band gap, seen in Fig. 4. A detailed analysis can be given in terms of the molecular orbitals (MO) associated with these two states and the spin density. Both introduced band-gap states, which are the highest (lowest) occupied (unoccupied) MOs of the interface structure, are fully localized around the unpassivated Si, in contrast to the next lower (higher) band state. Furthermore, the spin density is not only localized around the central Si atom but also exhibits a significant spread onto the back-bonded Si atoms. Overall this suggests a (slightly distorted) sp^3-hybridized Si dangling bond.

To better understand the individual bonding configurations along the trajectory, we also analyzed the charges associated with the involved Si and H atoms by using Mulliken population analysis as well as the method of Bader charge analysis. Both methods yield the same result: The H indeed dissociates in its neutral charge state with one remaining electron on the created Si-DB. All details are given in the Appendix.

2. *Trajectory 2:* Si–H → AB → $BC_{2,3}$

Additionally, we investigate trajectory 2, which involves the hydrogen invert into the AB position (3) and subsequently moves into the bond-center site formed between Si_2 and Si_3 (5). The CI-NEB results are shown in Fig. 5 together with the corresponding atomistic configurations. In an initial step the H bends into the $BC_{1,2}$ site which marks the first transition state in Fig. 5 with a reaction barrier of 2.2 eV. Thereby the Si_1–Si_2 distance increased by 0.64 Å to form the BC configuration. Subsequently, the H relaxes into the metastable AB site.

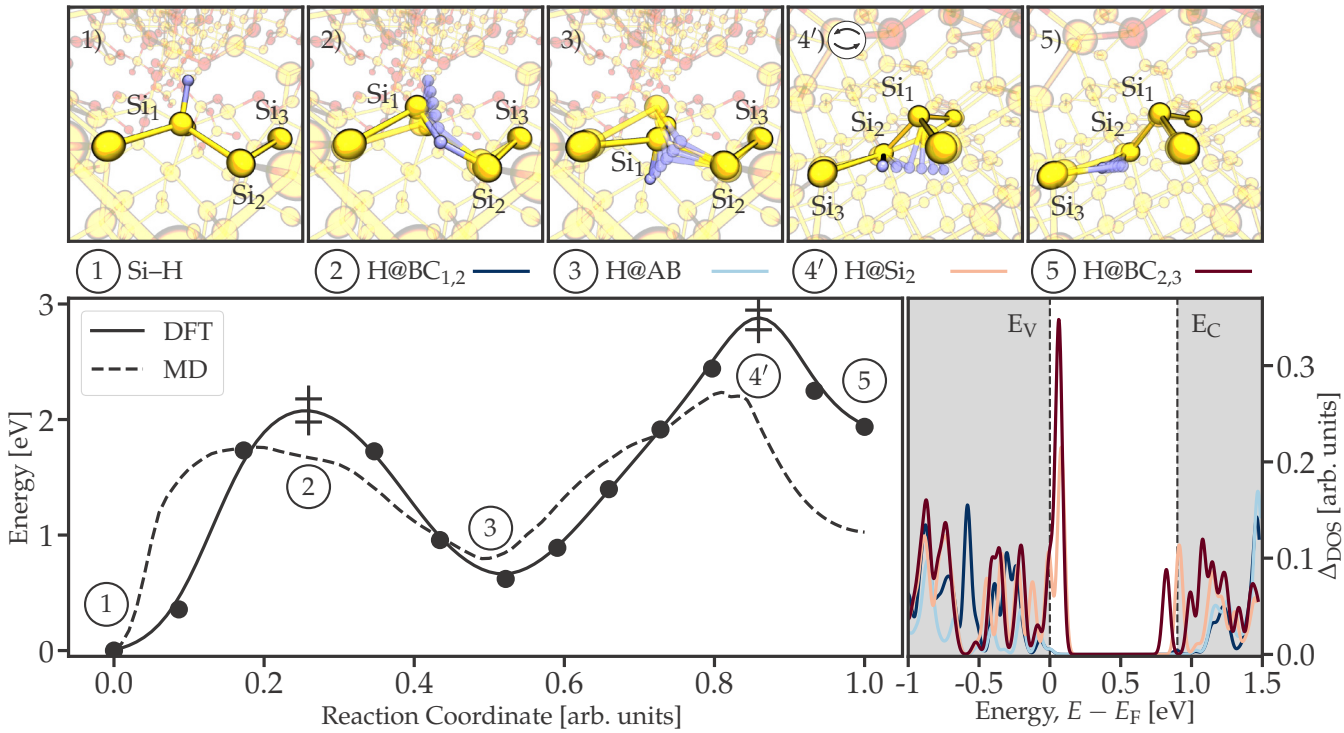

FIG. 5. The results of CI-NEB simulations bending the hydrogen from its equilibrium position (1) through the plane of an adjacent Si_1–Si_2 bond (2) into an inverted AB configuration (3). The energy barrier to overcome is 2.2 eV without any additional minimum along the path. Most importantly, one can see that no electronic states appear in the band gap at any position along the path from (1) to (3), indicating that the Si–H bond remains intact. Moving the H from the AB site (3) into the $BC_{2,3}$ configuration (5) proceeds over the transition state (4′) where the H is attached to Si_2 with a reaction barrier of 2.25 eV. This additional path indeed creates defect levels in the band gap of silicon, see Fig. 4.

Such a trajectory was also investigated by Tuttle and Van de Walle with a similar energy profile [33,39] and suggested to provide a possible pathway for H desorption. In particular, they suggested that the H in the AB configuration leads to energy levels in the Si band gap, which, upon charge capture, would lead to the breaking of the Si–H bond. However, as can be seen in the bottom right panel in Fig. 5, which shows the change in the projected density of states (pDOS) onto Si_1 compared to the equilibrium Si–H configuration, no additional states in the Si band gap are formed for positions (2) and (3). Thus, the results suggest that such a transition does not allow the Si–H complex to become charged and/or dissociate.

Therefore, we further investigated the trajectory connecting state (3) and (5), the bond-center configuration between Si_2 and Si_3, which is shown as the dotted line in Fig. 3. Figure 5 shows the corresponding energy with a reaction barrier of 2.25 eV relative to (3) formed by the transition state (4′), where the hydrogen is attached to Si_2. This path indeed creates localized electronic states in the band gap of silicon, as can be seen in the analysis of the DOS and is already mentioned above.

Quite reassuringly, the qualitative behavior of both results, the DFT as well as the MD simulations (shown in Fig. 3), is rather similar and predicts the same kinetics for the hydrogen. This can be seen best when the H moves from (3) towards state (4′). Even the *ab initio* simulations show that the lattice relaxation—particularly pronounced for Si_1—necessary to reach the AB site must be partially reversed to move the H towards Si_2. However, note that although the classical MD simulations predict a unique transition state (4) (Fig. 3) for both paths, (1)→(5) and (3)→(5), the CI-NEB simulations found two distinct configurations. While in both transition states the H is attached to Si_2 with a distance of 1.65 Å (4) and 1.68 Å (4′), respectively, the position of H with respect to Si_2 differs, as can be seen in Figs. 5 and 4.

Summarizing our results suggests the following: To break a Si–H bond at the Si/SiO_2 interface and create an electrically active Si dangling bond, the hydrogen needs to move into a stable BC site between the next but one Si–Si bond, e.g., Si_2 and Si_3. We propose the direct path connecting state (1) and (5) to be the preferred dissociation trajectory due to the slightly reduced reaction barrier and the lattice relaxations involved compared to the pathway including the AB site as an intermediate state.

IV. STATISTICAL ANALYSIS

Structural disorder at the Si/SiO_2 interface results in a distribution of Si–Si (and Si–O) bond lengths and angles. Thus, linking theoretical data and experimental results requires a statistical comparison. For our analysis we used three different Si/a-SiO_2 models, see Sec. II, and in total 13 variations of pristine Si–H bonds which were consistent with P_b center configurations. The Si–H configurations were created by breaking and passivating selected Si–Si or Si–O bonds and thus, also include P_{b1}-like types [see Fig. 2(a)] and configurations with nearby H atoms [see Fig. 2(b)]. In order to facilitate comparison with experimental results, which suggest

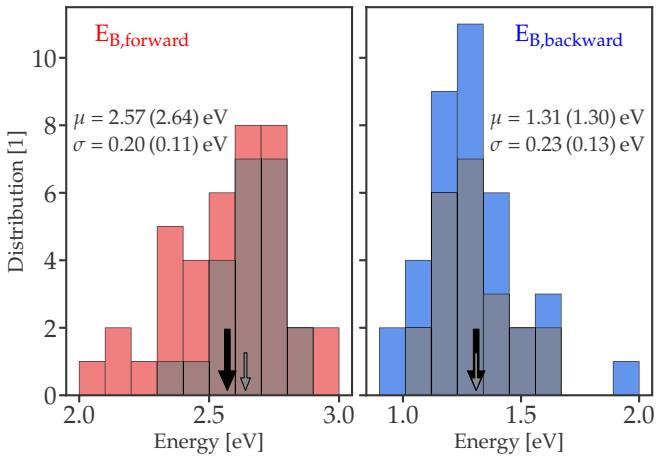

FIG. 6. Distribution of calculated barriers using the CI-NEB method. The statistics includes 38 simulated dissociation paths for various initial Si–H configurations, see Fig. 2. While the colored bars show the full result, the gray bars present a limited statistics, where the initial configuration is at least one layer away from the interface and properly reflects the characteristics of Fig. 2(c).

that the dominant defect at the (100)Si/SiO_2 interface is a Si-DB back bonded to three other Si atoms, all initial Si–H bonds are placed within 4 Å of the subinterfacial Si side. The three next-nearest $BC_{2,3}$ sites were chosen, and the direct trajectory was calculated using the CI-NEB method. Overall, 38 dissociation paths have been calculated and analyzed, see Fig. 6. We note that owing to computational limitations the CI-NEB simulations have been performed using the PBE functional. Subsequently, single point calculations based on the hybrid PBE0 functional were carried out on the optimized structures along the trajectory. The final results are shown in Fig. 6.

The calculated defect creation trajectories show a broad distribution of barriers to break or repassivate the Si–H bond, ranging from 2.07 (0.95) to 2.95 eV (1.94 eV) with a standard deviation of 0.20 and 0.23 eV, respectively. Mean values for both barriers are in good agreement with recent experimental studies, averaging at 2.57 eV (exp. 2.83 eV) for the forward reaction and 1.31 eV (exp. 1.51 eV) for the backward barrier. However, the calculated standard deviations σ are actually larger than extracted by measurements (exp. $\sigma_{B,f} = 0.08$ eV, $\sigma_{B,b} = 0.06$ eV). One possible reason for the wide distribution of barriers is the spatial position of the Si–H bond. Our statistics also includes Si–H bonds directly at the Si/SiO_2 interface, where Si atoms experience the maximum distortion due to the amorphous oxide, see Fig. 1. Limiting the statistics to the initial Si–H configuration residing in an interfacial Si environment, which means at least one layer away from the Si/SiO_2 transition, results in a much narrower distribution of barriers, see Fig. 6 (gray bars). The concept that interface defects are more likely to be in the subinterfacial Si region was already mentioned in recent publications [19,84] and further validates this assumption.

From these statistical observations we conclude that the proposed dissociation pathway, where the hydrogen atoms move from an initial Si–H configuration into a bond-center site between the next-nearest Si-Si bond, is a good candidate to explain the defect creation process at Si/SiO_2 interfaces.

V. DISCUSSIONS AND CONCLUSIONS

We have investigated the pathways and barriers for dissociation of the Si–H bond at the Si/SiO_2 interface and examined different dissociation pathways to create a Si dangling bond defect. Due to its significant technological importance, the literature already offers a wealth of information. Experimental data correlated with the creation of a silicon dangling bond at the Si/SiO_2 interface by dissociating hydrogen show a reaction barrier of 2.83 ± 0.08 eV [21,83]. Despite extensive theoretical work by Tuttle *et al.* and Van de Walle *et al.*, who investigated hydrogen-related configurations in crystalline and amorphous silicon models [32–39], there is still no clear picture regarding the actual Si–H dissociation kinetics.

To explore the potential energy surface in the vicinity of the Si–H bond and identify possible dissociation pathways, we have applied well-tempered metadynamics. This method allows one to perform enhanced sampling in molecular dynamics simulations, aside from equilibrium configurations. Using a classical force field within these simulations, three distinct minimum configurations for the hydrogen could be found: the intact Si–H in its equilibrium configuration, the inverted bond known as the antibonding site (AB site), as well as a bond-center configuration (BC site) where a Si–H–Si complex is formed between the next-nearest Si–Si bond. The resulting minimum energy paths connecting the different minimum configurations were further investigated and confirmed by CI-NEB DFT simulations. Quite surprisingly, the qualitative behavior of the MEPs for both approaches is rather similar. Our analysis shows that the trajectory for bending the H into the AB site does not allow the Si–H bond to break, contrary to what was suggested by Tuttle *et al.* [33,34]. Flipping the H into the AB site increases the Si–H bond length from 1.46 to 1.51 Å while the Si–Si distances remained constant. The associated electronic state indeed shifted by ∼0.2 eV closer to the Si valence and conduction band edges; however, no state within the band gap appeared. Test calculation in bulk Si showed the same result, which further validates the presented results. However, we propose a dissociation pathway where the H moves along the direct MEP into the next but one BC site to be responsible for the creation of active defects at the Si/SiO_2 interface. Our data clearly show that the H dissociates in its neutral charge state and indeed creates a Si dangling bond with two states in the Si band gap, a filled state in the lower half, as well as an empty state in the upper half of the band gap. The final result yields a forward barrier of 2.77 eV and a barrier of 1.30 eV for the passivation of the Si dangling bond with the H. Both values are in very good agreement with experimental results published by Stesmans [83].

Additionally, due to the amorphous nature of SiO_2 and structural disorder at the Si/SiO_2 interface we performed a statistical analysis. We used three different interface models and 13 variations of pristine Si–H bond configurations placed within 4 Å of the subinterfacial Si side. CI-NEB calculations have been performed for the direct trajectory to the three next-nearest $BC_{2,3}$ sites, resulting in a total number of 38 dissociation pathways. The calculated mean values for the

forward and backward barrier average at 2.57 eV ± 0.20 eV and 1.31 eV ± 0.23 eV, respectively, which is in good agreement with experimental data (2.83 and 1.51 eV). Limiting the statistics to initial configurations within the subinterfacial Si region, as was mentioned in recent publications, results in a narrower distribution of barriers and further improves the agreement with experimental data, with $E_{\mathrm{B,forward}} = 2.64\,\mathrm{eV} \pm 0.11\,\mathrm{eV}$ and $E_{\mathrm{B,backward}} = 1.30\,\mathrm{eV} \pm 0.13\,\mathrm{eV}$.

ACKNOWLEDGMENTS

The work was supported in part by the Austrian Science Fund (FWF) under Project No. P 26382-N30, in part by the Austrian Research Promotion Agency (FFG, Take-Off Program) under Project No. 861022, and in part by the European Union's Horizon 2020 Research and Innovation Programme under Marie Sklodowska-Curie Grant Agreement No. 794950. A.L.S. acknowledges funds provided by the UK Engineering and Physical Sciences Research Council (EPSRC) under Grants No. EP/K01739X/1 and No. EP/P013503/1 and by the Leverhulme Trust RPG-2016-135. Furthermore, the authors acknowledge support from the Vienna Scientific Cluster for providing resources on the Austrian high-performance cluster VSC3.

APPENDIX

A. Metadynamics simulations

In total 30 well-tempered metadynamics simulations with bias factors between 80 and 180 as well as bias heights ranging from 9 to 20 meV were conducted. The accessible region during the simulations was limited, as can be seen in the upper panel of Fig. 7. It should be noted that simulations with large bias factors and/or heights did not converge properly, and no reasonable free-energy surface could be extracted. However, simulations with smaller values (bias factors 80/90, bias heights 9–10 meV) indeed converged to the unique potential landscape shown in Fig. 3. The simulation result used in Sec. III was obtained by performing 50×10^6 time steps with a step size of 0.5 fs. In total, the added bias consisted of 1×10^5 Gaussian functions, each with a width of 0.5 Å and a height of 9 meV, which was used to calculate the free-energy surface. The bottom panel of Fig. 7 assesses the convergence of the simulation by showing the minimum energy path as a function of the simulation time. It can be clearly seen that the reconstructed paths for the 20- and 25-ns simulation time are almost on top of each other, thereby indicating the convergence of the simulation.

B. Charge analysis

The complex dissociation pathway proposed in Sec. III, which involves the interaction of the bending and stretching mode of the Si–H bond, requires a detailed understanding of the charge states of the corresponding atoms. Thus, we applied Mulliken population analysis as well as Bader charge [85–88] analysis to quantify the total electronic charge associated with the atoms. Both methods show that the hydrogen would actually dissociate in its neutral charge state, with one remaining electron on the Si dangling bond. This is clearly visible in Fig. 4, a filled state associated with the dangling bond in the lower half of the band gap and an empty state in the upper half.

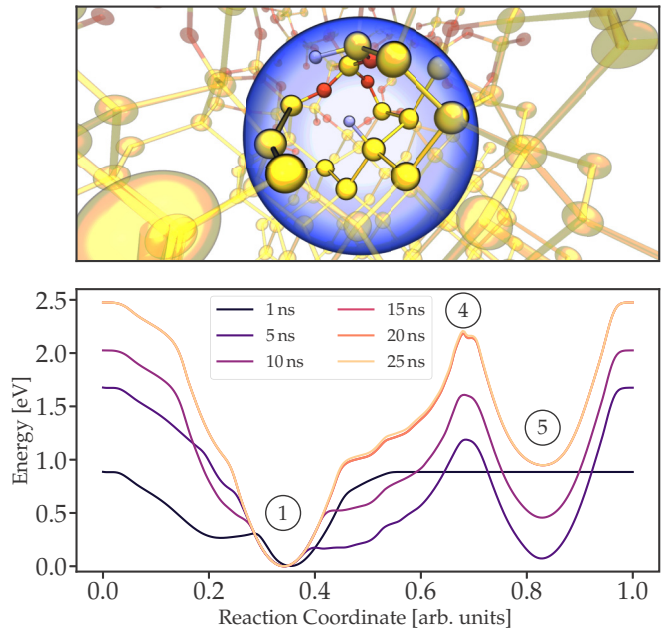

FIG. 7. Details of the well-tempered metadynamics simulations. The accessible spatial region during the simulation is shown as the blue sphere in the upper panel. It includes the subinterfacial regions on either side of the Si/SiO_2 interface. The lower panel assesses the convergence of the final simulation results. While for a 1-ns simulation time only the direct vicinity of the equilibrium configuration is explored, the minimum energy path connecting 1 and 5 barely changes between 20 and 25 ns, which indicates the convergence of the simulation run.

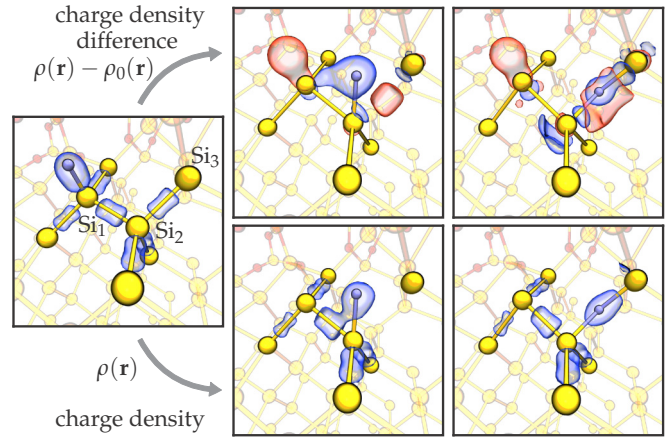

FIG. 8. The charge density is represented by the blue and red translucent profiles along the dissociation path (blue: increase of charge density, red: decrease of charge density). In the initial step the H attaches to an adjacent Si atom (Si_2) with a distance of 1.57 Å. Thereby, one electron remains on the initial Si_1 as indicated by the Bader charge analysis. In the final configuration the H forms a Si–H–Si complex between the next-nearest Si_2–Si_3 bond, as shown in the right panels. Being in this position, the H is slightly negatively charged and nearly fully bonded to Si_3 suggested by the charge density as well as the distances to Si_2 and Si_3.

Details of the Bader charge analysis are given in Fig. 8. The evolution (lower panels) as well as the change (upper panels) of the electronic density are shown at selected points along the dissociation pathway. One can clearly see that the H moves from the initial Si_1 to an intermediate configuration at the top of the transition barrier, where it is bound to the neighboring Si_2 and subsequently into its final BC position between Si_2 and Si_3. Integration of the associated Bader volumes of Si_1 shows that the charge associated with it changes by $0.78e$ as the H migrates to Si_2, and by $0.95e$ for the H being in its final position. This indicates that one electron remains on the Si dangling bond created during this process. Analyzing the H along the trajectory shows that its charge changes by $0.18e$, becoming slightly negatively charged in its final position. However, from this we conclude that the H would dissociate in its neutral charge state. Another important detail we want to note is the final position of the hydrogen atom. Along the trajectory the H first attaches to Si_2 until it moves to its final position between Si_2 and Si_3, which is already mentioned in the literature [38,40,89–91] to be a stable position for H^0. However, a closer look reveals that the H would actually be bound to Si_3, as suggested by the electronic density, see Fig. 8. This is also reflected by the distances between the H and the respective Si atoms. While at the transition point the H is 1.65 Å from the Si_2, this distance increases to 1.68 Å for the final position, compared to 1.55 Å between the H and Si_3. Thus, Si_2 also possesses the character of a Si dangling bond with one unpaired electron. However, no additional states in the Si band gap are created, which we assume is due to the interaction with the nearby H atom moving its energy level below the valence band. Within this context, it would be of interest to further investigate the effect of external charges onto the final Si–H–Si complex, as already mentioned in the Discussion.

[1] Y. Wimmer, A.-M. El-Sayed, W. Gös, T. Grasser, and A. L. Shluger, Proc. R. Soc. London, Sec. A **472**, 20160009 (2016).
[2] A.-M. El-Sayed, M. B. Watkins, T. Grasser, V. V. Afanas'ev, and A. L. Shluger, Phys. Rev. Lett. **114**, 115503 (2015).
[3] A.-M. El-Sayed, Y. Wimmer, W. Goes, T. Grasser, V. V. Afanas'ev, and A. L. Shluger, Phys. Rev. B **92**, 014107 (2015).
[4] A.-M. El-Sayed, M. B. Watkins, T. Grasser, V. V. Afanas'ev, and A. L. Shluger, Microelectron. Eng. **147**, 141 (2015).
[5] M. Kaviani, V. V. Afanas'ev, and A. L. Shluger, Phys. Rev. B **95**, 075117 (2017).
[6] P. Lenahan, Microelectron. Eng. **69**, 173 (2003).
[7] F. Cerbu, O. Madia, D. V. Andreev, S. Fadida, M. Eizenberg, L. Breuil, J. G. Lisoni, J. A. Kittl, J. Strand, A. L. Shluger, V. V. Afanas'ev, M. Houssa, and A. Stesmans, Appl. Phys. Lett. **108**, 222901 (2016).
[8] M. Stuckelberger, R. Biron, N. Wyrsch, F.-J. Haug, and C. Ballif, Renewable Sustainable Energy Rev. **76**, 1497 (2017).
[9] S. R. Schofield, P. Studer, C. F. Hirjibehedin, N. J. Curson, G. Aeppli, and D. R. Bowler, Nat. Commun. **4**, 1649 (2013).
[10] B. Naydenov and J. J. Boland, Nanotechnology **24**, 275202 (2013).
[11] L. Gao, P. P. Pal, T. Seideman, N. P. Guisinger, and J. R. Guest, J. Phys. Chem. Lett. **7**, 486 (2016).
[12] A. Stesmans and V. V. Afanas'ev, Appl. Phys. Lett. **82**, 4074 (2003).
[13] A. Stesmans and V. V. Afanas'ev, Phys. Rev. B **57**, 10030 (1998).
[14] K. Keunen, A. Stesmans, and V. V. Afanas'ev, Phys. Rev. B **84**, 085329 (2011).
[15] K. Kato, T. Yamasaki, and T. Uda, Phys. Rev. B **73**, 073302 (2006).
[16] E. H. Poindexter, P. J. Caplan, B. E. Deal, and R. R. Razouk, J. Appl. Phys. **52**, 879 (1981).
[17] A. Stesmans and V. V. Afanas'ev, J. Phys.: Condens. Matter **10**, L19 (1998).
[18] P. M. Lenahan and J. F. Conley, J. Vac. Sci. Technol., B: Microelectron. Nanometer Struct.–Process., Meas., Phenom. **16**, 2134 (1998).
[19] A. Stesmans, B. Nouwen, and V. Afanas'ev, Phys. Rev. B **58**, 15801 (1998).
[20] A. Stesmans, J. Appl. Phys. **88**, 489 (2000).
[21] K. L. Brower, Phys. Rev. B **42**, 3444 (1990).
[22] J. W. Lyding, K. Hess, and I. C. Kizilyalli, Appl. Phys. Lett. **68**, 2526 (1996).
[23] P. Avouris, R. Walkup, A. Rossi, H. Akpati, P. Nordlander, T.-C. Shen, G. Abeln, and J. Lyding, Surf. Sci. **363**, 368 (1996).
[24] P. Avouris, R. Walkup, A. Rossi, T.-C. Shen, G. Abeln, J. Tucker, and J. Lyding, Chem. Phys. Lett. **257**, 148 (1996).
[25] M. Bina, S. Tyaginov, J. Franco, K. Rupp, Y. Wimmer, D. Osintsev, B. Kaczer, and T. Grasser, IEEE Trans. Electron Devices **61**, 3103 (2014).
[26] S. Tyaginov, M. Jech, J. Franco, P. Sharma, B. Kaczer, and T. Grasser, IEEE Electron Device Lett. **37**, 84 (2016).
[27] C. Guerin, V. Huard, and A. Bravaix, J. Appl. Phys. **105**, 114513 (2009).
[28] A. Bravaix, Y. M. Randriamihaja, V. Huard, D. Angot, X. Federspiel, W. Arfaoui, P. Mora, F. Cacho, M. Saliva, C. Besset, S. Renard, D. Roy, and E. Vincent, in *2013 IEEE International Reliability Physics Symposium (IRPS)* (IEEE, New York, 2013), pp. 2D.6.1–2D.6.9.
[29] T. Grasser, M. Waltl, Y. Wimmer, W. Goes, R. Kosik, G. Rzepa, H. Reisinger, G. Pobegen, A. El-Sayed, A. Shluger, and B. Kaczer, in *2015 IEEE International Electron Devices Meeting (IEDM)* (IEEE, New York, 2015), pp. 20.1.1–20.1.4.
[30] T. Grasser, M. Waltl, K. Puschkarsky, B. Stampfer, G. Rzepa, G. Pobegen, H. Reisinger, H. Arimura, and B. Kaczer, in *2017 IEEE International Reliability Physics Symposium (IRPS)* (IEEE, New York, 2017), pp. 6A–2.1–6A–2.6.
[31] A. T. Krishnan, S. Chakravarthi, P. Nicollian, V. Reddy, and S. Krishnan, Appl. Phys. Lett. **88**, 153518 (2006).
[32] B. Tuttle and J. B. Adams, Phys. Rev. B **56**, 4565 (1997).
[33] B. Tuttle and C. G. Van de Walle, Phys. Rev. B **59**, 12884 (1999).
[34] B. Tuttle, Phys. Rev. B **60**, 2631 (1999).
[35] B. Tuttle, Phys. Rev. B **61**, 4417 (2000).
[36] B. R. Tuttle, D. R. Hughart, R. D. Schrimpf, D. M. Fleetwood, and S. T. Pantelides, IEEE Trans. Nucl. Sci. **57**, 3046 (2010).
[37] C. G. Van De Walle, Phys. Rev. B **49**, 4579 (1994).
[38] C. G. Van De Walle and R. A. Street, Phys. Rev. B **49**, 14766 (1994).

[39] C. Van de Walle and B. Tuttle, IEEE Trans. Electron Devices **47**, 1779 (2000).
[40] A. A. Bonapasta, Phys. B (Amsterdam, Neth.) **170**, 168 (1991).
[41] N. M. Johnson, C. Herring, and C. G. Van de Walle, Phys. Rev. Lett. **73**, 130 (1994).
[42] N. H. Nickel, G. B. Anderson, N. M. Johnson, and J. Walker, Phys. Rev. B **62**, 8012 (2000).
[43] K. Hess, Phys. B (Amsterdam, Neth.) **272**, 527 (1999).
[44] B. Tuttle, K. Hess, and L. Register, Superlattices Microstruct. **27**, 441 (2000).
[45] B. R. Tuttle, W. McMahon, and K. Hess, Superlattices Microstruct. **27**, 229 (2000).
[46] J. VandeVondele, M. Krack, F. Mohamed, M. Parrinello, T. Chassaing, and J. Hutter, Comput. Phys. Commun. **167**, 103 (2005).
[47] J. VandeVondele and J. Hutter, J. Chem. Phys. **127**, 114105 (2007).
[48] S. Goedecker, M. Teter, and J. Hutter, Phys. Rev. B **54**, 1703 (1996).
[49] M. Guidon, J. Hutter, and J. VandeVondele, J. Chem. Theory Comput. **5**, 3010 (2009).
[50] M. Guidon, J. Hutter, and J. VandeVondele, J. Chem. Theory Comput. **6**, 2348 (2010).
[51] C. G. Broyden, J. Appl. Math. **6**, 76 (1970).
[52] R. Fletcher, Comput. J. **13**, 317 (1970).
[53] D. Goldfarb, Math. Comput. **24**, 23 (1970).
[54] D. F. Shanno, Math. Comput. **24**, 647 (1970).
[55] R. Elber and M. Karplus, Chem. Phys. Lett. **139**, 375 (1987).
[56] G. Henkelman, B. P. Uberuaga, and H. Jónsson, J. Chem. Phys. **113**, 9901 (2000).
[57] S. Ling, A. M. El-Sayed, F. Lopez-Gejo, M. B. Watkins, V. V. Afanas'Ev, and A. L. Shluger, Microelectron. Eng. **109**, 310 (2013).
[58] L. Gerrer, S. Ling, S. M. Amoroso, P. Asenov, A. L. Shluger, and A. Asenov, J. Comput. Electron. **12**, 638 (2013).
[59] U. Khalilov, E. C. Neyts, G. Pourtois, and A. C. T. van Duin, J. Phys. Chem. C **115**, 24839 (2011).
[60] U. Khalilov, G. Pourtois, S. Huygh, A. C. T. van Duin, E. C. Neyts, and A. Bogaerts, J. Phys. Chem. C **117**, 9819 (2013).
[61] M. H. Evans, M. Caussanel, R. D. Schrimpf, and S. T. Pantelides, J. Comput. Electron. **6**, 85 (2007).
[62] R. Buczko, S. J. Pennycook, and S. T. Pantelides, Phys. Rev. Lett. **84**, 943 (2000).
[63] E. Kobeda and E. A. Irene, J. Vac. Sci. Technol., B: Microelectron. Process. Phenom. **5**, 15 (1987).
[64] E. P. EerNisse, Appl. Phys. Lett. **35**, 8 (1979).
[65] H. W. Conru, J. Appl. Phys. **47**, 2079 (1976).
[66] R. J. Jaccodine and W. A. Schlegel, J. Appl. Phys. **37**, 2429 (1966).
[67] S. C. H. Lin and I. Pugacz-Muraszkiewicz, J. Appl. Phys. **43**, 119 (1972).
[68] Y. Sugita, S. Watanabe, N. Awaji, and S. Komiya, Appl. Surf. Sci. **100-101**, 268 (1996).
[69] S. Miyazaki, H. Nishimura, M. Fukuda, L. Ley, and J. Ristein, Appl. Surf. Sci. **113-114**, 585 (1997), Proceedings of the Eighth International Conference on Solid Films and Surfaces.
[70] K. Hirose, H. Nohira, T. Koike, K. Sakano, and T. Hattori, Phys. Rev. B **59**, 5617 (1999).
[71] A. C. Diebold, D. Venables, Y. Chabal, D. Muller, M. Weldon, and E. Garfunkel, Mater. Sci. Semicond. Process. **2**, 103 (1999).
[72] N. Miyata, H. Watanabe, and M. Ichikawa, Phys. Rev. B **58**, 13670 (1998).
[73] D. A. Muller, T. Sorsch, S. Moccio, F. H. Baumann, K. Evans-Lutterodt, and G. Timp, Nature (London) **399**, 758 (1999).
[74] D. A. Muller and G. D. Wilk, Appl. Phys. Lett. **79**, 4195 (2001).
[75] Y. Yamashita, S. Yamamoto, K. Mukai, J. Yoshinobu, Y. Harada, T. Tokushima, T. Takeuchi, Y. Takata, S. Shin, K. Akagi, and S. Tsuneyuki, Phys. Rev. B **73**, 045336 (2006).
[76] C. Kaneta, T. Yamasaki, T. Uchiyama, T. Uda, and K. Terakura, Microelectron. Eng. **48**, 117 (1999), Insulating Films on Semiconductors.
[77] J. H. Oh, H. W. Yeom, Y. Hagimoto, K. Ono, M. Oshima, N. Hirashita, M. Nywa, A. Toriumi, and A. Kakizaki, Phys. Rev. B **63**, 205310 (2001).
[78] J. C. Fogarty, H. M. Aktulga, A. Y. Grama, A. C. T. van Duin, and S. A. Pandit, J. Chem. Phys. **132**, 174704 (2010).
[79] H. Aktulga, J. Fogarty, S. Pandit, and A. Grama, Parallel Comput. **38**, 245 (2012).
[80] See Supplemental Material at http://link.aps.org/supplemental/10.1103/PhysRevB.100.195302 for a detailed geometrical analysis of the utilized interface models, including the atomistic models as XYZ files, and a discussion of the different types of defects.
[81] Y. Yu, B. Wang, M. Wang, G. Sant, and M. Bauchy, J. Non-Cryst. Solids **443**, 148 (2016).
[82] G. A. Tribello, M. Bonomi, D. Branduardi, C. Camilloni, and G. Bussi, Comput. Phys. Commun. **185**, 604 (2014).
[83] A. Stesmans, Phys. Rev. B **61**, 8393 (2000).
[84] A. Stesmans and V. V. Afanas'ev, J. Appl. Phys. **83**, 2449 (1998).
[85] G. Henkelman, A. Arnaldsson, and H. Jónsson, Comput. Mater. Sci. **36**, 354 (2006).
[86] S. Hashmi and S. Al-Salam, Int. J. Clin. Exp. Pathol. **8**, 8786 (2015).
[87] W. Tang, E. Sanville, and G. Henkelman, J. Phys.: Condens. Matter **21**, 084204 (2009).
[88] M. Yu and D. R. Trinkle, J. Chem. Phys. **134**, 064111 (2011).
[89] C. G. Van de Walle, P. J. H. Denteneer, Y. Bar-Yam, and S. T. Pantelides, Phys. Rev. B **39**, 10791 (1989).
[90] C. G. Van de Walle and R. A. Street, Phys. Rev. B **51**, 10615 (1995).
[91] C. G. V. de Walle, J. Non-Cryst. Solids **227-230**, 111 (1998).